NANO LETTERS

pubs.acs.org/NanoLett Letter

Buckling-Mediated Phase Transitions in Nano-Electromechanical Phononic Waveguides

SunPhil Kim,[‖] Jonathan Bunyan,[‖] Paolo F. Ferrari,[‖] Ali Kanj,[‖] Alexander F. Vakakis, Arend M. van der Zande,* and Sameh Tawfick*

Cite This: https://doi.org/10.1021/acs.nanolett.1c00764 Read Online

ACCESS | Metrics & More | Article Recommendations | Supporting Information

ABSTRACT: Waveguides for mechanical signal transmission in the megahertz to gigahertz regimes enable on-chip phononic circuitry, which brings new capabilities complementing photonics and electronics. Lattices of coupled nano-electromechanical drumhead resonators are suitable for these waveguides due to their high Q-factor and precisely engineered band structure. Here, we show that thermally induced elastic buckling of such resonators causes a phase transition in the waveguide leading to reversible control of signal transmission. Specifically, when cooled, the lowest-frequency transmission band associated with the primary acoustic mode vanishes. Experiments show the merging of the lower and upper band gaps, such that signals remain localized at the excitation boundary. Numerical simulations show that the temperature-induced destruction of the pass band is a result of inhomogeneous elastic buckling, which disturbs the waveguide's periodicity and suppresses the wave propagation. Mechanical phase transitions in waveguides open opportunities for drastic phononic band reconfiguration in on-chip circuitry and computing.

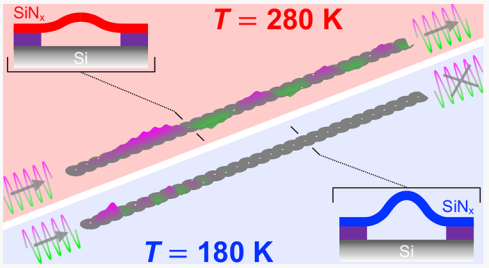

KEYWORDS: *waveguide, buckling, metamaterials, NEMS, phonon, nonlinearity*

Unidirectional lattices made from mechanically coupled arrays of nano-electromechanical systems' (NEMS) resonators act as high-Q phononic waveguides, which support mechanical signal processing at megahertz to gigahertz frequencies and, hence, can couple signals in the elastic, radio frequency, and optical domains.[1] These recent concepts have been used in photonic-phononic memory[2] and integrated circuitry.[3,4] These coupled NEMS oscillators also present opportunities in tuning[5] and topological systems.[6] However, despite these advancements, on-chip phononic waveguides mostly rely on the linear elastic nature of microfabricated materials and structures and take limited advantage of the exquisite behavior of strongly nonlinear mechanics and acoustics.

Indeed, elastic nonlinearity induces unusual acoustic wave transmission behaviors in mechanical metamaterials, the macroscale analogue of phononic crystals.[7,8] For instance, contact nonlinearity governs the dynamics of granular materials leading to solitary waves,[9] switching, and rectification.[10] Mechanically coupled buckling beams support elastic wave propagation and mechanical logic circuits.[11]

Structural phase transitions—in the metamaterial sense—are associated with a nonlinear buckling or distortion of the unit cell. Structural phase transitions are exploited in macroscale mechanical metamaterials to reconfigure their morphology, elastic response, or phononic band structures. For instance, phase-change materials such as chalcogenides are commonly used in memory devices[12] due to the large change in resistance associated with their phase transition. The application of these same concepts to mechanical metamaterials for use in specific applications is still in its infancy. Recent demonstrations of structural phase transitions in micro- or macroscale mechanical metamaterials exploit the elastic reorientation of the unit cell to control their static elastic response,[13,14] with applications in switching. Several reports demonstrate that buckling in macroscale acoustic metamaterials effectively controls the dynamic band structure with applications in vibration control.[15−17] Theoretical studies show that the coupling between the unit cells can lead to unusual behaviors like crossovers from a positive to negative group velocity.[18] However, combining these concepts to show reconfiguration (vs tuning) of a band structure in microsystems has not yet been demonstrated. Leveraging these proposed ideas to realize phase transitions in waveguides operating in the megahertz regime would enable advanced concepts such as traveling wave photonic-phononic translator (PPT),[19] which relies on the on-the-fly coupling/decoupling of coherent photonic-phononic waves for multidomain information processing, in thermal management systems,[20,21] and unravels new opportunities such

Received: February 23, 2021
Revised: July 19, 2021

as the switching and storage of mechanical signals through localization.

In this study, we exploit a thermally driven elastic buckling to strongly reconfigure the band structure and wave transmission in a one-dimensional phononic crystal, that is, a NEMS waveguide. The structural phase change is associated with a critical temperature and mechanical stress, and it not only reconstructs the band structure of the NEMS waveguide but also completely inhibits transmission via the fundamental acoustic band. Owing to the NEMS size scale, this coordinated buckling-induced phase transition is conveniently induced by a practical temperature change of 10 K. This contrasts with current common wisdom, which regards elastic instabilities as a nuisance in NEMS, leading to unpredictable behaviors and device variability.[22]

Figure 1 shows the considered one-dimensional lattice, consisting of coupled silicon nitride (SiN_x) drumhead

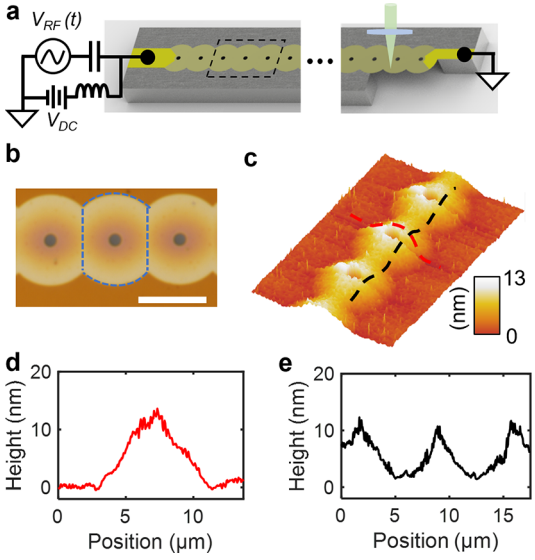

Figure 1. Design and structure of the phononic waveguide (W1). (a) Schematic drawing of the phononic waveguide along with the electrostatic actuation and optical detection apparatus. (b) Optical image of the waveguide. The image shows interferometric rings in the SiN_x membrane due to the out-of-plane deflection. The dotted line represents a unit cell. Scale bar = 7 μm. (c) Isometric topography map of the waveguide acquired using an atomic force microscope, showing an out-of-plane deflection. (d, e) Topographic profiles taken along the lines shown in (c) corresponding to the profile (d, red) perpendicular to and (e, black) along the waveguide. The SiN_x membrane's maximum deflection is 13 ± 2 nm.

resonators, having also been used in previous studies.[4,5,23] The lattice is composed of 61 suspended circular SiN_x films having a 60 nm nominal thickness suspended over a silicon substrate by a 150 nm thick silicon dioxide supporting layer. An advantage of this construction is that it utilizes standard semiconductor processes with no novel materials, which allows for the construction of on-die integrated phononic structures. We probe the phononic band structure of the waveguide by an electrostatic actuation at one end, while varying the device temperature between room temperature (RT) and 80 K. Figure 1a represents a schematic drawing of a waveguide along with the electrostatic actuation via a Cr−Au electrode deposited on the first and last unit cells in the waveguide and optical detection.[24,25]

Figure 1b shows an optical image of the waveguide where the dotted line represents a unit cell. Each unit cell within the waveguide is a circular membrane with an outer diameter of 9.7 μm, with a small 1.2 μm release hole at the center. The pitch between the membranes is 7 μm, so adjacent circular membranes overlap by 1.35 μm, forming a lattice of elastically coupled unit cells. The spacing and geometric parameters of the waveguide determine the resulting band structure. Each unit cell shows a faint interferometric ring, corresponding to a nonuniform distance between the membrane and the underlying silicon substrate.

Figure 1c shows an isometric topography map of the waveguide measured by atomic force microscopy (AFM). Figure 1d,e shows the profiles along and across the waveguide, as indicated by the black and red dotted lines in Figure 1c. In this waveguide device (W1), the maximum deflection at the center of the unit cell is 13 ± 2 nm. All cells show the same degree of deflection within the waveguide. This initial deflection at room temperature is a result of bending in the membrane under a compression from a residual thin-film stress, due to an asymmetric taper in the membrane thickness. We note that this study used commercially purchased nitride films, so we did not have a deterministic control over the film stress. Supporting Information Figure S1 shows the cross-sectional scanning electron microscopy (SEM) image of a waveguide with the thickness of the membrane varying as a continuous taper from 50 nm at the center of the chip to 65 nm at the outer edge. This taper in the thickness is caused by an imperfect selectivity in the etchant chemistry and breaks the symmetry of the membrane. Importantly, as detailed in the Supporting Information Section S2 and later simulations, this initial deflection is not due to buckling but is, instead, due to the bending moment resulting from the compression of the asymmetrically tapered membrane. This initial out-of-plane deformation is elastically stable (similar to the deflection of a cantilever beam due to an inclined compressive load). Under an additional compression, the membrane will undergo an elastic buckling instability transition. This causes a smooth transition between the prebuckled and postbuckled states as the membrane is compressed versus the sudden transition of an ideal symmetric structure. As a result, in our simulations and interpretation, we must treat the waveguide as a membrane under an initial deflection, a common case in buckling mechanics and NEMS.

We report on three representative waveguides, which we label W1, W2, and W3. First, we investigate the dynamic band structure of waveguide W1 at room temperature. Figure 2a shows the frequency response probed on the middle cell (#30) due to an excitation of cell #1. This waveguide displays three pass bands and two band gaps over the measured range. Band 1 spans 12.8−13.7 MHz, Band 2 spans 21.7−33.1 MHz, and Band 3 starts at 36 MHz. The band gap between bands 1 and 2 is 8 MHz, while the band gap between bands 2 and 3 is 2.9 MHz. This band structure is robust, yet the exact bounding frequencies vary with the fabrication conditions, as evidenced by measurements on the other waveguides (Supporting Information Figure S2). To understand the nature of these bands, we extract the amplitude and phase of all unit cells of the waveguide during the actuation at a specified frequency and Fourier-transform the spatial data to the reciprocal space. Figure 2b shows the band dispersion inside the first Brillouin zone, while Figure 2c shows the details of the first band. The

https://doi.org/10.1021/acs.nanolett.1c00764
Nano Lett. XXXX, XXX, XXX−XXX

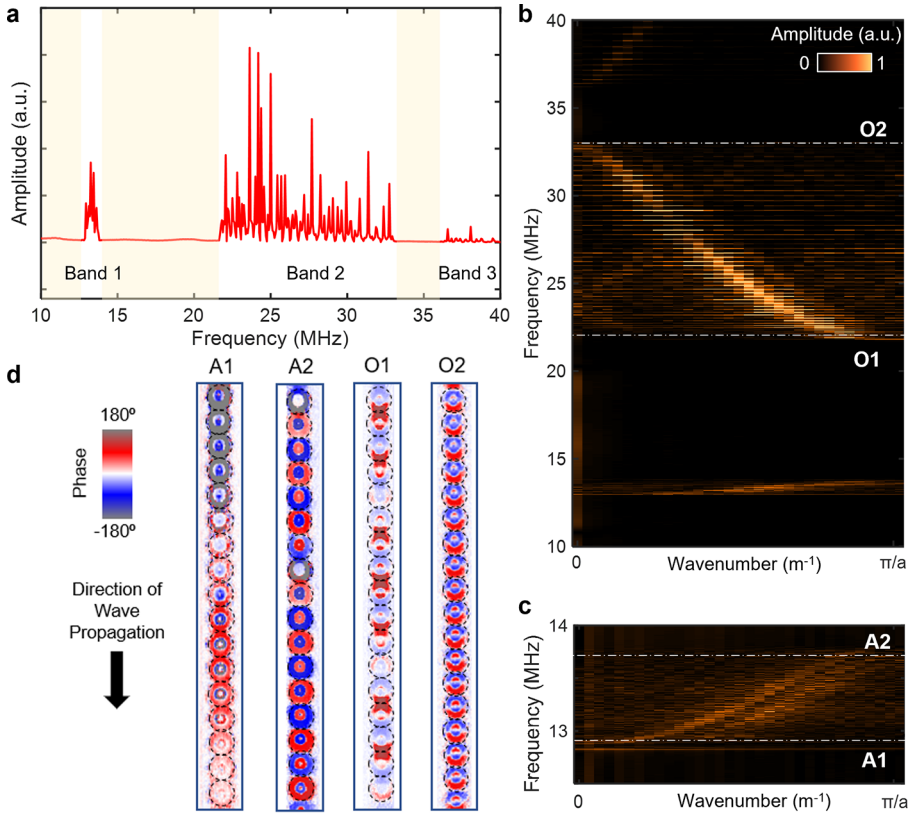

Figure 2. Phononic band structure of the waveguide (W1) at room temperature. (a) Frequency response of the unit cell at the center of the waveguide. Three bands are evident in this picture. As shown in (b), these bands correspond to the acoustic, optical, and a higher acoustic band. (b) Band dispersion of the waveguide obtained by the discrete Fourier transform of the amplitude response collected at every unit cell, where $a = 7$ μm is the unit cell pitch of the waveguide. The color scale is the magnitude of the transformed signal corresponding to a certain wavenumber for each particular frequency. (c) Detailed plot of the dispersion at the first band showing its acoustic character (positive dispersion). The white dashed lines indicate the frequencies at which mode mapping is performed. (d) Phase mappings of the waveguide for different frequencies. The modes A1 (12.8 MHz) and A2 (13.7 MHz) correspond to the lower and upper edges of the acoustic band, respectively, as indicated in (c). Similarly, modes O1 (22 MHz) and O2 (33 MHz) are located at the lower and upper edges of the optical band as shown in (b).

analysis of an additional waveguide from a different chip is presented in the Supporting Information Figure S3.

To further understand each band, we examine the Bloch modes at the band edges (i.e., the bounding frequencies of each band). We perform a spatial mapping of the modes by rastering the laser along the waveguide while driving at a fixed frequency and monitoring the dynamic amplitude and phase at each position (unit cell) with a lock-in amplifier. Figure 2d shows spatially resolved phase maps of the Bloch wave propagation at A1 (12.8 MHz) and A2 (13.7 MHz) for the acoustic band and O1 (22 MHz) and O2 (33 MHz) for the optical band. We observe a consistent behavior with Bloch waves, with a short-wavelength component at the level of the unit cells and a long-wavelength component distributed over many unit cells, corresponding to the wavenumber of the mode. As expected, the low-wavenumber modes correspond with the low-frequency acoustic (A1) and the high-frequency optical (O2) band edges. Conversely, the high-wavenumber modes correspond with the high-frequency acoustic (A2) and low-frequency optical (O1) band edges. In the same device tested after a few days, we mapped the Bloch modes taken at intermediary frequencies inside the bands (Supporting Information Figure S4), showing wavelengths corresponding to few unit cells. We note that the frequencies drift slightly in the span of days. By examining the repeating mode shapes in each unit cell, the first two bands are composed of Bloch waves rising from the first and second Bloch modes of each unit cell (also validated in COMSOL simulations discussed in Figure 4b). At room temperature, the band dispersion is similar to previous waveguide studies.[4,5,23]

The in situ observation of the membrane deflection due to temperature changes is enabled by our optical setup (Figure 3a). As the temperature is lowered, we observe the deflection of the membrane due to light interference between the membrane and the substrate. From the same underlying principle of the dynamic resonance measurements, the sensitivity of the optical contrast to interferometry enables the detection of deflections with sub-nanometer sensitivity. The right insets of Figure 3a show optical images of the waveguide deflection at 290 and 140 K, while the left schematic illustrates qualitatively the expected change in deflection. This deflection is indicative of thermoelastic buckling due to cooling-induced compressive stresses resulting from the mismatch of the coefficient of thermal expansion (CTE), α, between the nitride membrane and the underlying silicon substrate. Discussed further in the Supporting Information Section S3, for $\alpha_{SiNx} < \alpha_{Si}$, cooling leads to buckling.

Along with the buckling, we observe an unusual reconfiguration of the phononic band structure. Temperature-dependent frequency responses of waveguide W2 (similar to Figure 2a) are combined to construct Figure 3b. The extracted band edge

https://doi.org/10.1021/acs.nanolett.1c00764
Nano Lett. XXXX, XXX, XXX−XXX

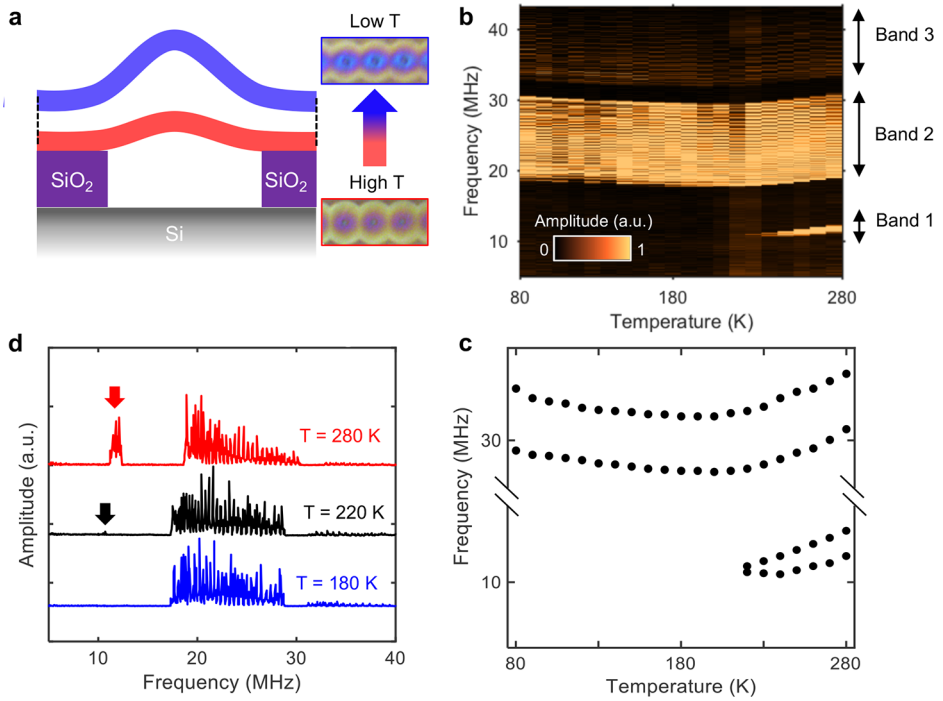

Figure 3. Effect of temperature on the frequency response of the phononic waveguide (W2). (a) Illustration of the buckled SiN_x films with cooling (left). Optical image of the waveguide at RT and at 140 K indicating a change in the out-of-plane deflection (right). These images were captured inside the cryostat used for the measurement. (b) Two-dimensional map of measured response vs frequency and temperature for the buckled waveguide. V_{RF} = 0 dBm, V_{DC} = 2 V, and laser power = 50 μW are kept constant during the measurement. Color scale is the measured dynamic optical reflectance, which is a convolution of the amplitude of motion and changes in the optical interferometric path. (c) Extracted frequency band edges for Bands 1, 2, and 3 vs temperature. The vertical dashed line represents the critical temperature, where the lowest pass band vanishes, and the direction of the frequency tuning changes. (d) Frequency responses for three temperatures: T = 280, 220, and 180 K. The frequency responses are artificially shifted in the vertical direction for visualization purposes.

frequencies are plotted in Figure 3c. Remarkably, the first acoustic band gradually narrows as the temperature is cooled, until we no longer detect any signal below 220 K; this is shown in the frequency responses at 280, 220, and 180 K of Figure 3d. Below the critical transition of 220 K, there is no observable wave transmission, suggesting the inactivity of the acoustic band. This phenomenon is robust and observed on four other waveguides (Supporting Information Figures S2 and S3), though variations from the fabrication process affect the exact band frequencies and transition temperatures. Furthermore, the second pass band shows continuous tuning, with a kink in the direction near the buckling transition around 220 K. The frequency tuning and kink of the second pass band are consistent with the thermomechanical buckling of individual circular plates and beams with an initial small deflection.[26,27] Under a more negative stress (increasing compression), the frequency of the second pass band of a flat or initially deflected membrane decreases, until the resonator reaches the critical compression to buckle.[27−32] Once in the postbuckled state, the second pass frequency rises with additional in-plane compression due to an increase in the total bending. To our knowledge, such a complete inhibition of wave transmission through the acoustic band has not been previously reported.

To unravel the effect of temperature on the buckling of the individual cells and the reconfiguration of the band structure, we performed two types of dynamic simulations using finite element method. The first simulation type considers a single unit cell with periodic boundary conditions, which we use to calculate the acoustic band structure including the effect of cooling-induced buckling. The second type of simulations is on a finite length waveguide, consisting of 60 unit cells similar to the waveguide used in the experiments to reveal a buckling-induced aperiodicity in the waveguide, which leads to suppression of the band transmission.

Figure 4a shows the simulated static deflection of the center point of a single unit cell with periodic boundary conditions as a function of the applied temperature change ΔT. The simulated material is assigned a negative coefficient of thermal expansion (CTE) $\approx (\alpha_{SiNx} - \alpha_{Si}) < 0$ to account for the difference in contraction between the silicon and the nitride during cooling due to the isothermal equilibrium within the chip. With a negative CTE, a cooling of the simulated unit cell (i.e., $\Delta T < 0$) induces compressive stresses due to the imposed clamping and periodic boundary conditions depicted in the inset of Figure 4a. Simulation details are present in Supporting Information Section S4 and Figure S6. Under the simulated cooling, the cell deflects into an out-of-plane equilibrium shape (at ΔT = −20, −120, and −180 K, corresponding to (**I**) before, (**II**) at, and (**III**) after the buckling transition, respectively). The buckling transition manifests as a kink in the deflection versus compression at case **II**. As noted earlier, a small bending-induced deflection before the buckling transition results from asymmetry.

Figure 4b shows the computed band structure of the three different cooling cases **I**, **II**, and **II** and the color-coded shapes of the corresponding eigenmodes, where the wavenumber of 0 m^{-1} is shown on the left and π/a is on the right (a being the unit cell width, cf. inset of Figure 4a). For each case, we simulated the band structure of the cooled waveguide by using the equilibrated static shape and imposing the Bloch periodic

https://doi.org/10.1021/acs.nanolett.1c00764
Nano Lett. XXXX, XXX, XXX−XXX

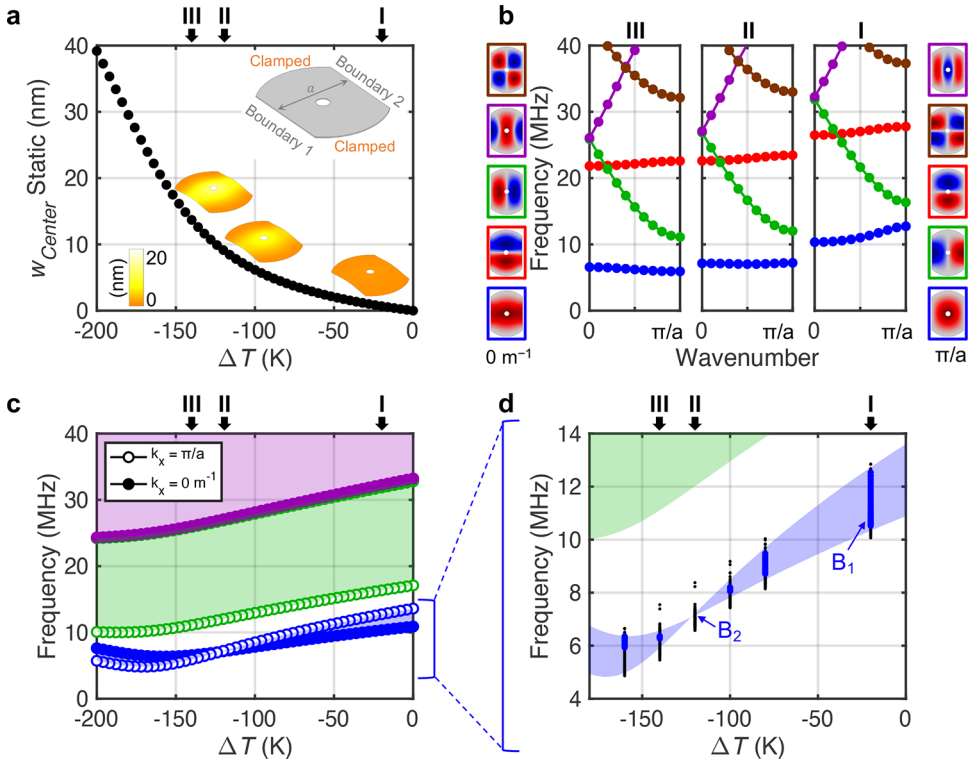

Figure 4. Numerical simulation of the buckling-induced phase transition. (a) Simulated transverse deflection of the membrane center (w_{Center}) under static equilibrium vs temperature change (ΔT). Top right inset depicts the simulated membrane. Insets next to the data points show the resulting equilibrium configuration for (from right to left): $\Delta T = -20$ K (**I**), -120 K (**II**), and -140 K (**III**). (b) Frequency dispersion curves vs wavenumber of the Bloch modes simulated for the three cases of stress: **I**, **II**, and **III**. Insets depict the mode shapes of the unit cell at different frequencies corresponding to the wavenumber limits of 0 m^{-1} (left) and π/a (right). (c) Simulated frequency limits (wavenumber $\in \{0\ m^{-1}, \pi/a\}$) for the considered values of temperature change. (d) Eigenfrequency (data points) of the finite system having 60 cells superimposed on top of the pass bands (the shaded regions) predicted by the Bloch modes of Figure 4c. The enlarged blue dots correspond to the eigenfrequencies that transmit waves based on the frequency sweep simulations (cf. Figure 5 and Supporting Information Figure S9). Labeled points B_1 and B_2 refer to the modes of the 60-cell system depicted in Figure 5f,g.

boundary condition (see the Supporting Information Section S4). At the prebuckled state, case **I**, the lowest pass band is the acoustic mode. At the buckling transition, case **II**, the acoustic pass band is flat. At the postbuckled state, case **III**, the first (lowest-frequency) band curvature inverts in comparison with case **I**, going from a positive to negative group velocity. In contrast, the higher bands only shift along the frequency axis.

We computationally track the evolution of the band structure under the effect of cooling and relate the numerical to the experimental findings. Figure 4c plots the bounding frequencies of each pass band at the wavenumber of 0 m^{-1} (solid circle) and π/a (open circle) as a function of temperature change ΔT. For a better visualization, we only plot the first (blue), second (green), and fourth bands (purple), chosen based on the modes most visible in the experimental measurements. Figure 4d shows an enlarged view of the frequency tuning of the first pass band, along with predictions of which modes will propagate from finite simulations discussed later.

Both the first mode and the higher modes qualitatively match the experimental measurements in Figure 3b. First, the direction of frequency tuning of all the bands (blue, green, purple) has a kink in direction near a critical crossover temperature. Second, the limiting frequencies of the first pass band (blue) have a different rate of tuning with cooling, which causes a continuous narrowing of the band, until there is a crossover at $\Delta T \approx -120$ K, corresponding to a transition from a positive to negative group velocity. The model does not match the precise experimentally measured frequencies, which is expected given that the band structure is sensitive to process parameters that were difficult to precisely control during the fabrication.

The kink in the pass bands near the critical temperature is reminiscent of the behavior of the individual eigenmodes in single membranes[29,31,32] and was observed more recently in the theoretical analysis of linear waveguides undergoing buckling.[33] This behavior confirms that a decreasing temperature leads to a compression and buckling of the individual unit cells. If the membrane thickness was constant and symmetric with respect to the neutral axis, this kink would be very sharp. However, a taper-induced asymmetry softens the influence of buckling on the frequency tuning. The periodic unit cell simulations show the narrowing and flattening of the acoustic band leading up to the buckling transition and the re-emergence of the acoustic pass band post-transition with a negative group velocity. This re-emergence is not observed in experiment. The simulation of the unit cell with periodic boundary conditions (i.e., Bloch modes), shown in Figure 4, captures most of the measured features of the band structure, except the loss of transmission at low temperatures. As the Supporting Information Figures S10 and S11 show, this behavior is robust over a wide range of stress states, including strong anisotropy, and is shown to be present for different geometries (Supporting Information Figure S12).

https://doi.org/10.1021/acs.nanolett.1c00764
Nano Lett. XXXX, XXX, XXX−XXX

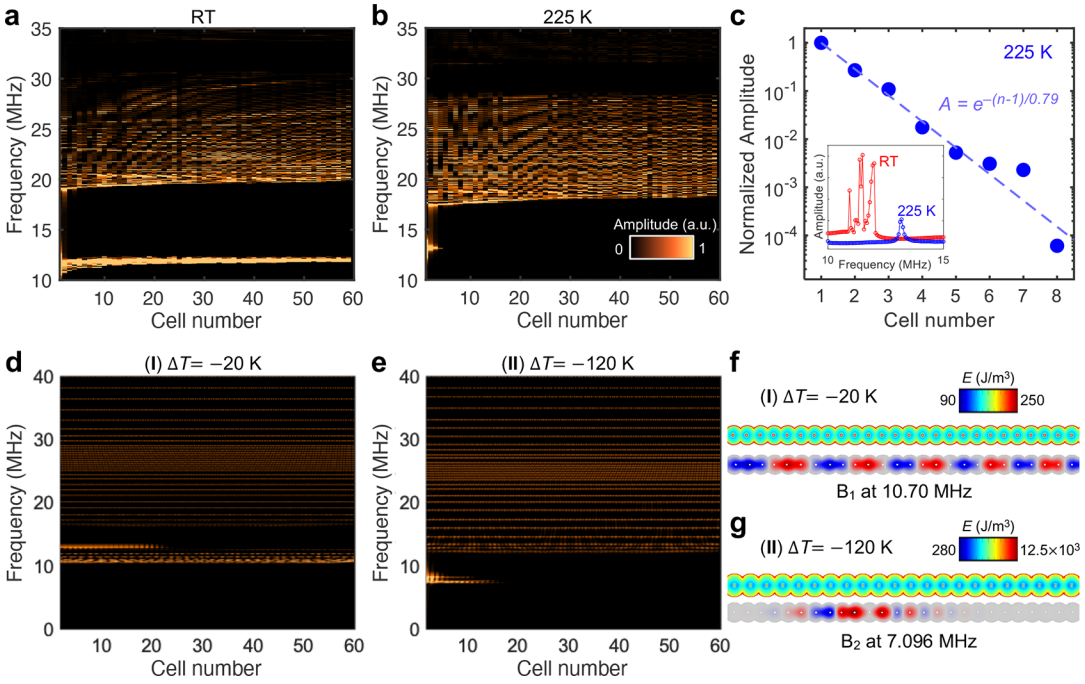

Figure 5. Spatial mapping of the frequency response as a function of temperature in the waveguide (W3) at (a) RT and (b) 225 K. The color scale is the measured dynamic optical reflectance scaled for clarity. The corresponding band dispersion curves are available in the Supporting Information Figure S3. (c) Spatial decay of the amplitude at 225 K. The extracted amplitudes are normalized with respect to the first unit cell (extracted frequencies are between 13.08 and 13.17 MHz). Inset: frequency response of the third (n = 3) unit cell at RT (red) and 225 K (blue). Spatial mapping of the frequency response simulated via COMSOL of the 60-cell waveguide at (d) prebuckling with ΔT = −20 K (**I**) and (e) postbuckling with ΔT = −120 K (**II**) (cf. Figure 4). The color map corresponds to the normalized steady-state amplitude of the transverse displacement due to the harmonic forcing with the respective frequency. (f, g) Color map on the top surface of cells from 5 to 30 (from left to right) showing (top) the residual strain energy density E resulting at a static equilibrium and (bottom) the mode shape of the indicated eigenmodes B_1 and B_2 on Figure 4c of the 60-cell waveguide simulated at (f) prebuckling with ΔT = −20 K (**I**) and (g) near critical buckling at ΔT = −120 K (**II**). In the eigenmode color maps, peaks and valleys are colored with blue and red, respectively; while nodes of zero displacement are colored with gray.

To understand the loss of transmission of the acoustic band, we compare the response of all the unit cells along a waveguide both experimentally and via simulations of the full 60 cell waveguide. Figure 5a shows the experimentally measured amplitude versus cell number at RT for a waveguide device (W3). We observe the transmission of energy through the entire waveguide for all bands. As shown in Figure 5b, when the temperature is lowered below the critical transition to 225 K, there is no transmission along the first band, and energy is localized to only the first few unit cells. Figure 5c plots the log-scale amplitude versus the unit cell number of the lowest band at 13.2 MHz at 225 K. The inset shows the relative frequency response of the lowest band in the third unit cell at room temperature and at 225 K. Below the transition, the first few unit cells show a single resonance corresponding to the excitation of the first unit cell. An exponential decay in amplitude occurs along the waveguide with a decay length of 0.79 unit cells. These data, along with the mode mappings shown in the Supporting Information Figure S5, indicate that the buckling of the unit cells does not strongly affect the modes of individual unit cells but strongly affects the transmission of waves along the waveguide.

Next, we simulate the frequency response of a finite waveguide formed by 60 unit cells. We explore two geometries, namely, (1) waveguides where all the membranes have the same thickness profiles and (2) waveguides having a small thickness gradient expected to result from a 5% variation in the etching rate (cf. Supporting Information Figure S7). As expected, the uniform thickness waveguide fully agrees with the infinite periodic system shown in Figure 4. The simulations of the waveguides with thickness gradient are more insightful. Figure 5d,e shows the simulated amplitude vs cell number at −20 and −120 K for the 60-cell waveguide with a thickness gradient. As shown in Figure 4d, the frequency evolution of these modes is depicted as data points superimposed on the periodic simulation to show that the two simulation approaches quantitatively agree. However, by computing the full 60 cells, we discovered that some of the modes are localized and are not excited, because they do not extend across the waveguide. In close agreement with experiment, the simulation shows the waveguide transmits waves only within a narrower frequency range of the lower band predicted in Figure 4d (corresponding to acoustic modes) for ΔT = −20 K (Figure 5d) and then gradually loses transmission upon further cooling. We use ΔT = −20 K because the membranes are under a small stress at RT in the experiments as shown in Figure 1. Transmission is completely lost at ΔT = −120 K (Figure 5e). Hence, under strong compression and buckling (case **II** in Figure 4), the simulation of the finite waveguide with thickness gradient captures the experimentally observed loss of transmission in the acoustic band.

Taken together, the loss of transmission results from an aperiodic disorder, the effect of which is nonlinearly magnified at a higher compression and buckling. To further visualize the origin of the transmission loss, Figure 5f shows the strain energy density E distribution along the waveguide from Cell 5

https://doi.org/10.1021/acs.nanolett.1c00764
Nano Lett. XXXX, XXX, XXX−XXX

to 30 (of 60) induced by the simulated cooling at −20 K (**I**) and a representative eigenmode B_1 at the frequency of 10.7 MHz (point indicated in Figure 4d). Correspondingly, Figure 5e shows the strain energy density at the critical temperature of −120 K (**II**) and an eigenmode B_2 at the frequency of 7.096 MHz. In Figure 5f, the prebuckled case (**I**), the residual strain energy density E near the center etch holes is nearly periodic between the unit cells. Because the thickness gradient is only 5%, the gradient in energy density is very subtle. The eigenmode B1 is uniform and propagates along the entire waveguide. In contrast, Figure 5g shows a more pronounced gradient in E in case (**II**), where E is slightly lower toward the center of the waveguide (cell 30) which, while still small, effectively breaks the waveguide periodicity. This creates what resembles a global stress distribution spanning the length of the waveguide. This aperiodic residual strain energy affects the modes of the 60-cell system. For example, the simulated eigenmode B_2 is a localized nontransmitting mode (cf. Figure 5g). Supporting Information Figure S9 shows the frequency vs unit cell position at additional temperatures. The Supporting Information includes videos of the mode shape evolution for different frequencies and cooling ΔT. As shown in the Supporting Information Figure S8 and videos, we additionally show that a waveguide with uniform thickness transmits waves at values of compressive stresses.

The localized, nontransmitting modes are only observed for the first pass band acoustic modes (blue band in Figure 4d) and are believed to result from the global buckling-induced strain distribution along the waveguide. In contrast, higher-frequency bands transmit waves even postbuckling as illustrated by experiments and simulations (Figure 5b,e, respectively). We hypothesize that the reason only the first band is affected is due to the relative shape of the global stress distribution vs the eigenmodes. The fundamental mode corresponding with the first band has the same shape as the buckling or stress distribution of each unit cell. Static distributions and dynamic modes with similar shapes are strongly coupled due to effective projection from one shape onto the other. However, the dynamic eigenmodes in the higher-frequency bands are characterized by higher-order harmonics (i.e., having a different symmetry with additional nodes in each unit cell) and hence are nearly orthogonal (w.r.t. shape) to the global static stress distribution leading to weak coupling. We note that not all features are perfectly captured by the simulations. For example, the experimentally observed band gap between modes 2 and 3 does not appear in simulations. We hypothesize that these higher-order differences are due to an imperfect knowledge of system parameters or nonsimulated variations like gradients in diameter or initial stress along the waveguide.

Returning to Figure 4d, the dots show every predicted eigenfrequency of the waveguide in the first pass band. However, as seen in Figure 5g, many of these modes are localized. The bold blue dots show the modes that extend across the waveguide, while the remaining black dots indicate localized modes, which do not propagate waves. At a low compression (higher temperature), most of the modes propagate, while at a higher compression, the majority of modes is localized. In the postbuckled regime (**III**) there are some propagating modes. However, we note that the existence of propagating modes in the postbuckling regime is a function of the assumed etch gradient. Here we assumed a 5% gradient. For greater than 25% gradient all modes were localized at every temperature. In experiments, there are other sources of inhomogeneity, for example diameter changes from etch variations, which could easily suppress remaining modes.

The realization of engineered phase transitions in phononic waveguides can be further controlled and harnessed in advanced phononic devices. Precisely tailoring the phase transition temperature (e.g., close to room temperature) is readily attainable by controlling the stoichiometry and deposition stress of the SiN_x membranes. Alternatively, control of the buckling could be attained by an electrostatic gating, which would allow fast and on-demand reconfigurability in mechanical circuits. The summary of our new findings is that the loss of acoustic transmission, described as a phase transition, is a multiscale effect combining a nonlinear elastic buckling at the individual unit cell scale (local buckling) with an aperiodic residual stress distribution along the full waveguide scale. Integrating such waveguides into on-chip phononic circuits will realize topologically protected states, switches, delay lines, and persistent memory through a localization. Moreover, photonic and phononic traveling waves can be coupled/decoupled on demand to reconfigure the circuit connectivity. Accordingly, phase transitions in phononic NEMS devices provide a critical future capability for phononic and coupled multidomain computing.

■ ASSOCIATED CONTENT

Supporting Information

The Supporting Information is available free of charge at https://pubs.acs.org/doi/10.1021/acs.nanolett.1c00764.

- Comparisons of the simulated eigenmodes' normalized-transverse deflection at the waveguide's centerline in the uniform vs inhomogeneous buckled waveguide TT= −20 T after cooling by ΔT = −20 K (MP4)
- Comparisons of the simulated eigenmodes' normalized-transverse deflection at the waveguide's centerline in the uniform vs inhomogeneous buckled waveguide after cooling by ΔT = −80 K (MP4)
- Comparisons of the simulated eigenmodes' normalized-transverse deflection at the waveguide's centerline in the uniform vs inhomogeneous buckled waveguide after cooling by ΔT = −100 K (MP4)
- Comparisons of the simulated eigenmodes' normalized-transverse deflection at the waveguide's centerline in the uniform vs inhomogeneous buckled waveguide after cooling by ΔT = −120 K (MP4)
- Methods of sample fabrication and measurement; discussion of buckling in asymmetric membranes; review of the SiN_x coefficients of thermal expansion; simulation details and table of simulation parameters; discussion of simulation robustness; additional figures (PDF)

■ AUTHOR INFORMATION

Corresponding Authors

Arend M. van der Zande − *Department of Mechanical Science and Engineering and Materials Research Laboratory, University of Illinois at Urbana−Champaign, Urbana, Illinois 61801, United States;* orcid.org/0000-0001-5104-9646; Email: arendv@illinois.edu

Sameh Tawfick − *Department of Mechanical Science and Engineering, University of Illinois at Urbana−Champaign, Urbana, Illinois 61801, United States;* orcid.org/0000-0003-3645-527X; Email: tawfick@illinois.edu

https://doi.org/10.1021/acs.nanolett.1c00764
Nano Lett. XXXX, XXX, XXX−XXX

Authors

SunPhil Kim − *Department of Mechanical Science and Engineering, University of Illinois at Urbana−Champaign, Urbana, Illinois 61801, United States;* Present Address: Molecular Foundry, Lawrence Berkeley National Laboratory, Berkeley, CA 94720 USA; orcid.org/0000-0002-5627-1139

Jonathan Bunyan − *Department of Mechanical Science and Engineering, University of Illinois at Urbana−Champaign, Urbana, Illinois 61801, United States;* orcid.org/0000-0001-7177-0481

Paolo F. Ferrari − *Department of Mechanical Science and Engineering, University of Illinois at Urbana−Champaign, Urbana, Illinois 61801, United States;* orcid.org/0000-0001-9787-553X

Ali Kanj − *Department of Mechanical Science and Engineering, University of Illinois at Urbana−Champaign, Urbana, Illinois 61801, United States;* orcid.org/0000-0002-4449-0940

Alexander F. Vakakis − *Department of Mechanical Science and Engineering, University of Illinois at Urbana−Champaign, Urbana, Illinois 61801, United States*

Complete contact information is available at: https://pubs.acs.org/10.1021/acs.nanolett.1c00764

Author Contributions

S.P.K. identified the transmission loss in the waveguides at low temperatures under A.v.d.Z.'s supervision. J.B. designed and fabricated the waveguides under S.T. and A.V's supervision. P.F.F. performed the spatial mapping and band structure measurements under A.v.d.Z.'s supervision. A.K. performed the band structure simulations, under S.T. and A.V.'s supervision. All authors discussed the model to explain the results and read and contributed to the manuscript.

Author Contributions

‖These authors contributed equally.

Notes

The authors declare no competing financial interest.

■ ACKNOWLEDGMENTS

J.B., A.K., A.V., and S.T. acknowledge support from NSF Emerging Frontiers Research Initiative (EFRI) Grant No. 1741565. J.B. and S.T. acknowledge helpful discussions with J. Cha and C. Daraio. S.K., P.F.F., and A.v.d.Z. acknowledge support from NSF-CAREER Award No. CMMI-1846732. This work was performed in part in the Holonyak Micro and Nano Technology Laboratory (HMNTL), the Materials Research Laboratory (MRL) Central Facilities, and the Micro-Nano-Mechanical Systems Cleanroon at the University of Illinois. The authors acknowledge the use of facilities and instrumentation supported by the NSF through the University of Illinois Materials Research Science and Engineering Center Award No. DMR-1720633.

■ REFERENCES

(1) Balram, K. C.; Davanço, M. I.; Song, J. D.; Srinivasan, K. Coherent coupling between radiofrequency, optical and acoustic waves in piezo-optomechanical circuits. *Nat. Photonics* **2016**, *10*, 346−352.

(2) Merklein, M.; Stiller, B.; Vu, K.; Madden, S. J.; Eggleton, B. J. A chip-integrated coherent photonic-phononic memory. *Nat. Commun.* **2017**, *8*, 574.

(3) Fu, W.; Shen, Z.; Xu, Y.; Zou, C.-L.; Cheng, R.; Han, X.; Tang, H. X. Phononic integrated circuitry and spin-orbit interaction of phonons. *Nat. Commun.* **2019**, *10*, 2743.

(4) Hatanaka, D.; Mahboob, I.; Onomitsu, K.; Yamaguchi, H. Phonon waveguides for electromechanical circuits. *Nat. Nanotechnol.* **2014**, *9*, 520−524.

(5) Cha, J.; Daraio, C. Electrical tuning of elastic wave propagation in nanomechanical lattices at MHz frequencies. *Nat. Nanotechnol.* **2018**, *13*, 1016−1020.

(6) Cha, J.; Kim, K. W.; Daraio, C. Experimental realization of on-chip topological nanoelectromechanical metamaterials. *Nature* **2018**, *564*, 229−233.

(7) Hussein, M. I.; Leamy, M. J.; Ruzzene, M. Dynamics of Phononic Materials and Structures: Historical Origins, Recent Progress, and Future Outlook. *Appl. Mech. Rev.* **2014**, *66*, 040802.

(8) Kochmann, D. M.; Bertoldi, K. Exploiting Microstructural Instabilities in Solids and Structures: From Metamaterials to Structural Transitions. *Appl. Mech. Rev.* **2017**, *69*, 050801.

(9) Starosvetsky, Y.; Vakakis, A. F. Traveling waves and localized modes in one-dimensional homogeneous granular chains with no precompression. *Phys. Rev. E* **2010**, *82*, 026603.

(10) Boechler, N.; Theocharis, G.; Daraio, C. Bifurcation-based acoustic switching and rectification. *Nat. Mater.* **2011**, *10*, 665−668.

(11) Raney, J. R.; Nadkarni, N.; Daraio, C.; Kochmann, D. M.; Lewis, J. A.; Bertoldi, K. Stable propagation of mechanical signals in soft media using stored elastic energy. *Proc. Natl. Acad. Sci. U. S. A.* **2016**, *113*, 9722−9727.

(12) Wong, H. P.; Raoux, S.; Kim, S.; Liang, J.; Reifenberg, J. P.; Rajendran, B.; Asheghi, M.; Goodson, K. E. Phase Change Memory. *Proc. IEEE* **2010**, *98*, 2201−2227.

(13) Kochmann, D. M.; Bertoldi, K. Exploiting Microstructural Instabilities in Solids and Structures: From Metamaterials to Structural Transitions. *Appl. Mech. Rev.* **2017**, *69*, 050801.

(14) Jin, L.; Khajehtourian, R.; Mueller, J.; Rafsanjani, A.; Tournat, V.; Bertoldi, K.; Kochmann, D. M. Guided transition waves in multistable mechanical metamaterials. *Proc. Natl. Acad. Sci. U. S. A.* **2020**, *117*, 2319−2325.

(15) Bertoldi, K.; Boyce, M. C. Mechanically triggered transformations of phononic band gaps in periodic elastomeric structures. *Phys. Rev. B: Condens. Matter Mater. Phys.* **2008**, *77*, 052105.

(16) Wang, P.; Shim, J.; Bertoldi, K. Effects of geometric and material nonlinearities on tunable band gaps and low-frequency directionality of phononic crystals. *Phys. Rev. B: Condens. Matter Mater. Phys.* **2013**, *88*, 014304.

(17) Wang, P.; Casadei, F.; Shan, S.; Weaver, J. C.; Bertoldi, K. Harnessing Buckling to Design Tunable Locally Resonant Acoustic Metamaterials. *Phys. Rev. Lett.* **2014**, *113*, 014301.

(18) Park, H. W.; Oh, J. H. Study of Abnormal Group Velocities in Flexural Metamaterials. *Sci. Rep.* **2019**, *9*, 13973.

(19) Safavi-Naeini, A. H.; Painter, O. Proposal for an optomechanical traveling wave phonon-photon translator. *New J. Phys.* **2011**, *13*, 013017.

(20) Terraneo, M.; Peyrard, M.; Casati, G. Controlling the Energy Flow in Nonlinear Lattices: A Model for a Thermal Rectifier. *Phys. Rev. Lett.* **2002**, *88*, 094302.

(21) Seif, A.; DeGottardi, W.; Esfarjani, K.; Hafezi, M. Thermal management and non-reciprocal control of phonon flow via optomechanics. *Nat. Commun.* **2018**, *9*, 1207.

(22) Zande, A. M. v. d.; Barton, R. A.; Alden, J. S.; Ruiz-Vargas, C. S.; Whitney, W. S.; Pham, P. H. Q.; Park, J.; Parpia, J. M.; Craighead, H. G.; McEuen, P. L. Large-Scale Arrays of Single-Layer Graphene Resonators. *Nano Lett.* **2010**, *10*, 4869−4873.

(23) Hatanaka, D.; Dodel, A.; Mahboob, I.; Onomitsu, K.; Yamaguchi, H. Phonon propagation dynamics in band-engineered one-dimensional phononic crystal waveguides. *New J. Phys.* **2015**, *17*, 113032.

(24) Kim, S.; Yu, J.; van der Zande, A. M. Nano-electromechanical Drumhead Resonators from Two-Dimensional Material Bimorphs. *Nano Lett.* **2018**, *18*, 6686−6695.

(25) Kim, S.; Annevelink, E.; Han, E.; Yu, J.; Huang, P. Y.; Ertekin, E.; van der Zande, A. M. Stochastic Stress Jumps Due to Soliton Dynamics in Two-Dimensional van der Waals Interfaces. *Nano Lett.* **2020**, *20*, 1201−1207.
(26) Kim, C.; Dickinson, S. The flexural vibration of slightly curved slender beams subject to axial end displacement. *Journal of Sound and Vibration* **1986**, *104*, 170−175.
(27) Zhang, Y.; Hosono, S.; Nagai, N.; Hirakawa, K. Effect of buckling on the thermal response of microelectromechanical beam resonators. *Appl. Phys. Lett.* **2017**, *111*, 023504.
(28) Kramer, E.; van Dorp, J.; van Leeuwen, R.; Venstra, W. J. Strain-dependent damping in nanomechanical resonators from thin MoS2 crystals. *Appl. Phys. Lett.* **2015**, *107*, 091903.
(29) Park, J.-S.; Kim, J.-H.; Moon, S.-H. Thermal post-buckling and flutter characteristics of composite plates embedded with shape memory alloy fibers. *Composite Structures* **2004**, *63*, 179−188.
(30) Tawfik, M.; Ro, J.-J.; Mei, C. Thermal post-buckling and aeroelastic behaviour of shape memory alloy reinforced plates. *Smart Mater. Struct.* **2002**, *11*, 297−307.
(31) Park, J.-S.; Kim, J.-H.; Moon, S.-H. Thermal post-buckling and flutter characteristics of composite plates embedded with shape memory alloy fibers. *Composites, Part B* **2005**, *36*, 627−636.
(32) Li, S.-R.; Yu, W.-S.; Batra, R. C. Free Vibration of Thermally Pre/Post-Buckled Circular Thin Plates Embedded with Shape Memory Alloy Fibers. *Journal of Thermal Stresses* **2010**, *33*, 79−96.
(33) Nguyen, B. H.; Zhuang, X.; Park, H. S.; Rabczuk, T. Topologically switchable behavior induced by an elastic instability in a phononic waveguide. *J. Appl. Phys.* **2020**, *127*, 245109.

https://doi.org/10.1021/acs.nanolett.1c00764
Nano Lett. XXXX, XXX, XXX−XXX